LETTER

An ultraluminous X-ray source powered by an accreting neutron star

M. Bachetti[1,2], F. A. Harrison[3], D. J. Walton[3], B. W. Grefenstette[3], D. Chakrabarty[4], F. Fürst[3], D. Barret[1,2], A. Beloborodov[5], S. E. Boggs[6], F. E. Christensen[7], W. W. Craig[8], A. C. Fabian[9], C. J. Hailey[10], A. Hornschemeier[11], V. Kaspi[12], S. R. Kulkarni[3], T. Maccarone[13], J. M. Miller[14], V. Rana[3], D. Stern[15], S. P. Tendulkar[3], J. Tomsick[6], N. A. Webb[1,2] & W. W. Zhang[11]

The majority of ultraluminous X-ray sources are point sources that are spatially offset from the nuclei of nearby galaxies and whose X-ray luminosities exceed the theoretical maximum for spherical infall (the Eddington limit) onto stellar-mass black holes[1,2]. Their X-ray luminosities in the 0.5–10 kiloelectronvolt energy band range from 10^{39} to 10^{41} ergs per second[3]. Because higher masses imply less extreme ratios of the luminosity to the isotropic Eddington limit, theoretical models have focused on black hole rather than neutron star systems[1,2]. The most challenging sources to explain are those at the luminous end of the range (more than 10^{40} ergs per second), which require black hole masses of 50–100 times the solar value or significant departures from the standard thin disk accretion that powers bright Galactic X-ray binaries, or both. Here we report broadband X-ray observations of the nuclear region of the galaxy M82 that reveal pulsations with an average period of 1.37 seconds and a 2.5-day sinusoidal modulation. The pulsations result from the rotation of a magnetized neutron star, and the modulation arises from its binary orbit. The pulsed flux alone corresponds to an X-ray luminosity in the 3–30 kiloelectronvolt range of 4.9×10^{39} ergs per second. The pulsating source is spatially coincident with a variable source[4] that can reach an X-ray luminosity in the 0.3–10 kiloelectronvolt range of 1.8×10^{40} ergs per second[1]. This association implies a luminosity of about 100 times the Eddington limit for a 1.4-solar-mass object, or more than ten times brighter than any known accreting pulsar. This implies that neutron stars may not be rare in the ultraluminous X-ray population, and it challenges physical models for the accretion of matter onto magnetized compact objects.

The brightest accretion-powered X-ray pulsars, A0538−66[5], SMC X-1[6] and GRO J1744−28[7], are variable, with reported X-ray luminosities up to $L_X(2\text{–}20\,\mathrm{keV}) \approx 10^{39}\,\mathrm{erg\,s^{-1}}$, which are at the low end of the range that defines ultraluminous X-ray sources (ULXs). Such luminosities, exceeding the Eddington limit for a neutron star by a factor of about six, can be understood[8] as resulting from accretion of material at moderately super-Eddington rates through a disk that couples to the neutron star's strong dipolar magnetic field (surface fields of $B \approx 10^{12}\,\mathrm{G}$). At the magnetospheric (Alfvén) radius, material is funnelled along the magnetic axis, radiation escapes from the column's side, and radiation pressure is ineffective at arresting mass transfer[9,10]. Explaining ULXs that have $L_X > 10^{39}\,\mathrm{erg\,s^{-1}}$ with a $\sim 1 M_\odot$ compact object using typical accreting pulsar models is however extremely challenging[8].

The NuSTAR (Nuclear Spectroscopic Telescope Array) high energy X-ray mission[11] observed the galaxy M82 (at distance $d \approx 3.6\,\mathrm{Mpc}$) seven times between 2014 January 23 and 2014 March 06 as part of a follow-up campaign of the supernova SN 2014J. The galaxy's disk contains several

ULXs, the most luminous being M82 X-1[12], which can reach $L_X(0.3\text{–}10\,\mathrm{keV}) \approx 10^{41}\,\mathrm{erg\,s^{-1}}$, and the second brightest being a transient, M82 X-2 (also referred to as X42.3+59[13]), which has been observed to reach[4,14] $L_X(0.3\text{–}10\,\mathrm{keV}) \approx 1.8 \times 10^{40}\,\mathrm{erg\,s^{-1}}$. The two sources are separated by $5''$, and so can only be clearly resolved by the Chandra X-ray telescope. During the M82 monitoring campaign, NuSTAR observed bright emission from the nuclear region containing the two ULXs. The region shows moderate flux variability at the 20% level during the first 22 days of observation. The flux was then found to have decreased by 60% by the time of the final observation ~ 20 days later. The peak X-ray flux, $F_X(3\text{–}30\,\mathrm{keV}) = (2.33 \pm 0.01) \times 10^{-11}\,\mathrm{erg\,cm^{-2}\,s^{-1}}$ (90% confidence; Fig. 1) corresponds to a total 3–30 keV luminosity assuming isotropic emission of $3.7^{+0.01}_{-0.02} \times 10^{40}\,\mathrm{erg\,s^{-1}}$.

A timing analysis revealed a narrow peak just above the noise at a frequency of $\sim 0.7\,\mathrm{Hz}$ in the power density spectrum. An accelerated epoch folding search[15] on overlapping 30-ks intervals of data found coherent pulsations with a mean period P of 1.37 s modulated with a sinusoidal period of 2.53 days throughout the 10-day interval starting at modified Julian day (MJD) 56691 (2014 February 03), and also in the last observation at MJD 56720 (Fig. 1). The statistical significance of the pulsations is $\sim 13\sigma$ during the most significant 30-ks segments, and $>30\sigma$ for the entire observation. A refined analysis (see Methods) subsequently enabled the detection of pulsations over a longer interval beginning on MJD 56686. The pulsed flux is variable, ranging from 5% to 13% in the 3–30 keV range, and from 8% to 23% in the 10–30 keV range; see Fig. 1c. Although the pulsed flux increases with energy, this may result from a reduction in the contamination from other sources in the point-spread function rather than from a true increase in pulsed fraction. The maximum pulsed luminosity of the periodic source, which we will hereafter refer to as NuSTAR J095551+6940.8, is $4.9^{+0.02}_{-0.03} \times 10^{39}\,\mathrm{erg\,s^{-1}}$ (3–30 keV).

Analysis of the period modulation yields a near-circular orbit (upper eccentricity limit of 0.003; see Methods) with a projected semi-major axis of 22.225(4) light s (1σ error). In addition to the orbital modulation, a linear spin-up of the pulsar is evident, with a period derivative $\dot{P} \approx -2 \times 10^{-10}\,\mathrm{s\,s^{-1}}$ over the interval from MJD 56696 to 56701 when the pulse detection is most significant. Phase-connecting the observations enables detection of a changing spin-up rate over a longer timespan (Fig. 2a) as well as erratic variations likely to be related to local changes in the torque on the neutron star applied by accreting matter[16].

Chandra observed M82 from MJD 56690.8396 to 56692.618, during an epoch when pulsations are detected. Only two sources in the Chandra image, M82 X-1 and M82 X-2, are sufficiently bright to be the counterpart of NuSTAR J095551+6940.8 (see Methods). We find the centroid of the pulsed emission (right ascension $\alpha = 09\,\mathrm{h}\,55\,\mathrm{min}\,51.05\,\mathrm{s}$, declination
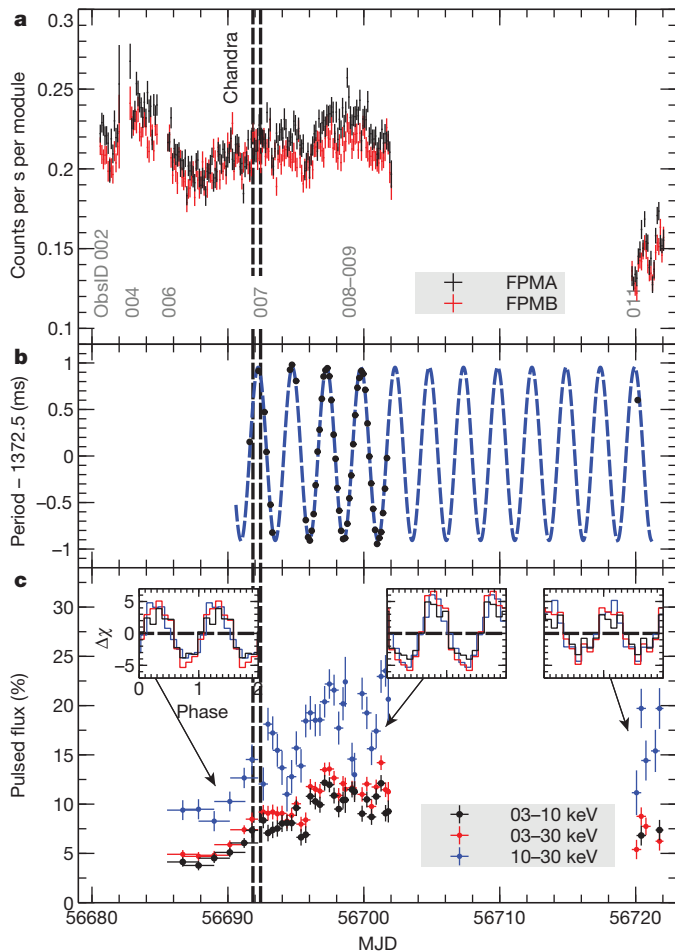
Figure 1 | The X-ray light curve and pulsations from the region containing NuSTAR J095551+6940.8. a, The background-subtracted 3–30 keV light curve extracted from a 70″-radius region around the position of NuSTAR J095551+6940.8. Black and red indicate the count rate from each of the two NuSTAR focal plane modules (FPMA and FPMB; 1σ errors). The vertical grey labels indicate different observations. **b**, Detection of the pulse period. Data (black points) are fitted using the best sinusoidal ephemeris (blue dashed line). The mean period is 1.37252266(12) seconds, with an orbital modulation period of 2.51784(6) days. The dashed vertical lines through all panels delineate the contemporaneous Chandra observation. **c**, Pulsed flux as a fraction of the emission from the 70″ region. Insets, pulse profile at indicated points, normalized so that $\sigma = 1$.

$\delta = +69°\,40'\,47.9''$) to be consistent with the location of M82 X-2 (Fig. 3). Monitoring by the Swift satellite establishes that the decrease in the nuclear region flux seen during observation (ObsID) 011 (see Extended Data Table 1) is due to fading of M82 X-1. The persistence of pulsations during this time further secures the association of the pulsating source, NuSTAR J095551+6940.8, with M82 X-2. We derive a flux $F_x(0.5–10\,\mathrm{keV}) = 4.07 \times 10^{-12}\,\mathrm{erg\,cm^{-2}\,s^{-1}}$, and an unabsorbed luminosity of $L_X(0.5–10\,\mathrm{keV}) = (6.6 \pm 0.1) \times 10^{39}\,\mathrm{erg\,s^{-1}}$ for M82 X-2 during the Chandra observation.

The detection of coherent pulsations, a binary orbit, and spin-up behaviour indicative of an accretion torque unambiguously identify NuSTAR J095551+6940.8 as a magnetized neutron star accreting from a stellar companion. The highly circular orbit suggests the action of strong tidal torques, which, combined with the high luminosity, point to accretion via Roche lobe overflow. The orbital parameters give a Newtonian mass function $f = 2.1M_\odot$ (here $M_\odot$ indicates the solar mass), and the lack of eclipses and assumption of a Roche-lobe-filling companion constrain the inclination to be $i < 60°$. The corresponding minimum companion mass assuming a $1.4M_\odot$ neutron star is $M_c > 5.2M_\odot$, with radius $R_c > 7R_\odot$.
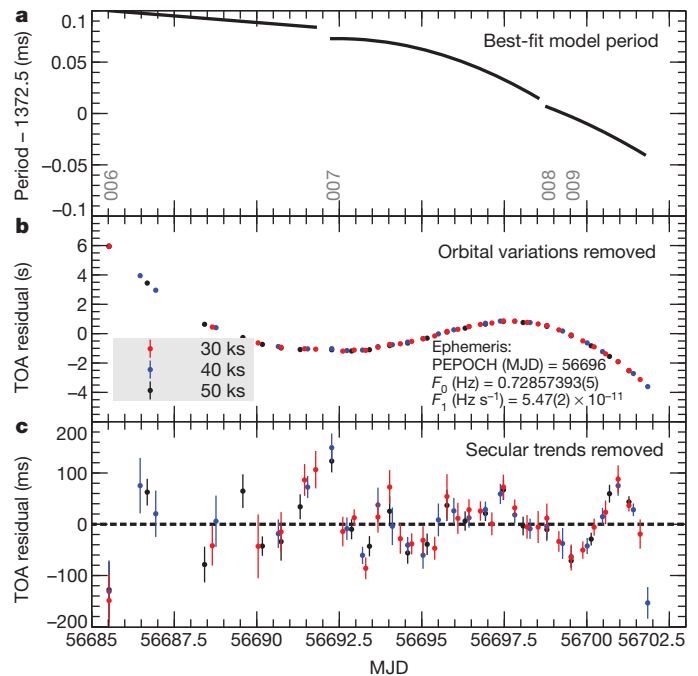

Figure 2 | The spin-up behaviour of NuSTAR J095551+6940.8. a, The residual period after correcting for the sinusoidal orbital modulation given in Extended Data Table 2. The period, displayed through the best-fit in Extended Data Table 3, decreases consistently, but the spin-up rate is changing. **b**, Time of arrival (TOA) residuals after removing the best-fit sinusoidal orbital modulation and a constant period derivative (the parameters are shown in commonly used units[26]). PEPOCH, F_0 and F_1 are the reference time and the pulse frequency and its derivative, respectively. There is a clear trend independent of the choice of time binning (30, 40 or 50 ks) that results from the variable spin-up. **c**, Residuals after a smooth curve is fitted to the TOA residuals. Residual noise remains in the TOAs at the 100 ms level (1σ uncertainties).

It is challenging to explain the high luminosity using standard models for accreting magnetic neutron stars. Adding the Chandra-measured $E < 10\,\mathrm{keV}$ luminosity to the $E > 10\,\mathrm{keV}$ pulsed flux (NuSTAR cannot directly spatially resolve the ULX), NuSTAR J095551+6940.8 has a luminosity $L_X(0.5–30\,\mathrm{keV}) \approx 10^{40}\,\mathrm{erg\,s^{-1}}$. Theoretically, the X-ray luminosity depends strongly on the magnetic field and the geometry of the accretion channel, being largest for a thin, hollow funnel that can result from the coupling of a disk onto the magnetic field[10]. A limiting luminosity $L_X \approx \dfrac{l_o}{2\pi d_o}L_{Edd}$, where l_o is the arc length of the funnel, d_o its thickness, and L_{Edd} the Eddington luminosity, can be reached if the magnetic field is high enough ($B \gtrsim 10^{13}\,\mathrm{G}$) to contain the accreting gas column[8]. Ratios of $l_o/d_o \approx 40$ are plausible, so that the limiting luminosity can reach $L_X \approx 10^{39}\,\mathrm{erg\,s^{-1}}$, implying mass transfer rates exceeding the Eddington value by many times. Beyond this, additional factors increasing L_X could result from increased L_{Edd} due to very high ($B > 10^{14}\,\mathrm{G}$) fields, which can reduce the electron scattering opacity[17], and/or a heavy neutron star. Some geometric beaming is also likely to be present.

This scenario is, however, difficult to reconcile with the measured rate of spin-up. The spin-up results from the torque applied by accreting material threading onto the magnetic field[18,19]. NuSTAR J095551+6940.8 is likely to be in spin equilibrium, given the short spin-up timescale, $P/\dot{P} \approx 300\,\mathrm{yr}$. Near equilibrium, the magnetosphere radius, r_m, is comparable to the co-rotation radius (the radius where a Keplerian orbit co-rotates with the neutron star):

$$r_{co} = \left(\frac{GM_{NS}P^2}{4\pi^2}\right)^{1/3} = 2.1 \times 10^8 \left(\frac{M_{NS}}{1.4M_\odot}\right)$$

Here G is the gravitational constant, M_{NS} is the neutron star mass, and r_{co} is in cm. With this assumption we can convert the measured torque,
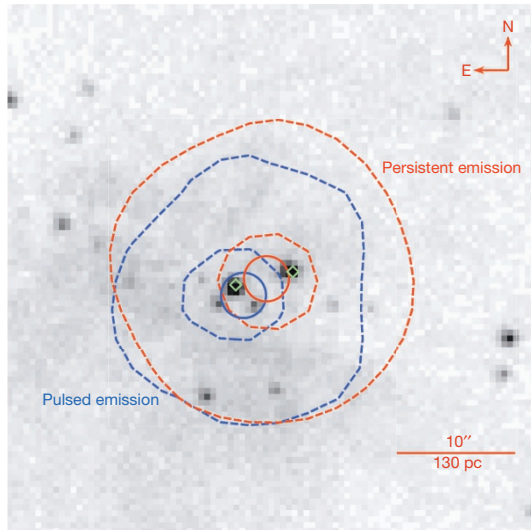
Figure 3 | The counterpart of NuSTAR J095551+6940.8. The greyscale image shows a 45″ × 45″ Chandra image of the galaxy's centre. Green diamonds mark the locations of M82 X-1 and X-2. NuSTAR 10–40 keV intensity contours (dashed) (50% and 90% levels) are shown for the pulsed (blue) and the persistent (red) emission. Solid error circles indicate the 3σ statistical uncertainty on the centroid locations (see Methods). The pulsed emission centroid is consistent with the location of M82 X-2, and the centroid of the persistent emission is between M82 X-1 and X-2, indicating that there is additional persistent emission from X-2 as well as the persistent emission from X-1.

$\tau = 2\pi I\dot{v} = 6 \times 10^{35} I_{45}\,\mathrm{g\,cm^2\,s^{-2}}$ (where I_{45} is the neutron star moment of inertia I (in units of $10^{45}\,\mathrm{g\,cm^2}$) and $\dot{v}$ is the measured frequency derivative) into a rate of matter magnetically channelled onto the pulsar:

$$\dot{M}_{\mathrm{mag}} = 5 \times 10^{-8} M_{1.4}^{-\frac{1}{2}} \left(\frac{r_{\mathrm{m}}}{r_{\mathrm{co}}}\right)^{-\frac{1}{2}} M_\odot\,\mathrm{yr}^{-1} = 2.5 \left(\frac{r_{\mathrm{m}}}{r_{\mathrm{co}}}\right)^{-\frac{1}{2}} \dot{M}_{\mathrm{Edd}}$$

where $M_{1.4}$ is the mass in units of 1.4 solar masses and $\dot{M}_{\mathrm{Edd}}$ is the Eddington accretion rate. From the spin-up we therefore find an accretion rate that is only a few times higher than Eddington, independent of any assumption about the pulsar magnetic field. For an equilibrium spin period of 1.37 s and $\dot{M} \approx \dot{M}_{\mathrm{Edd}}$, the implied magnetic field is $B \approx 10^{12}$ G, typical of accreting pulsars in high mass X-ray binaries, and too low to have an appreciable effect on L_{Edd}. It is possible that the current $\dot{M}$ is significantly larger than the average for this system, so that $r_{\mathrm{m}} < r_{\mathrm{co}}$, increasing $\dot{M}_{\mathrm{mag}}$. For $\dot{M} = 100\dot{M}_{\mathrm{avg}}$, $\dot{M}_{\mathrm{mag}}$ is increased tenfold, so that only moderate geometric beaming is required to explain the observed luminosity. A fan beam geometry[9] viewed at a favourable angle could in this case produce the observed pulse profile (Fig. 1) and provide the requisite moderate collimation.

The discovery of an ultraluminous pulsar has implications for understanding the ULX population. The fraction of ULXs powered by neutron stars must now be considered highly uncertain. M82 X-2 has been extensively studied[4,14], but pulsations have until now eluded detection owing to the limited timing capabilities of sensitive X-ray instruments, the transient nature of the pulsations, and the large amplitude of the orbital motion. Pulsars may indeed not be rare among the ULX population.

1. Roberts, T. P. X-ray observations of ultraluminous X-ray sources. *Astrophys. Space Sci.* **311,** 203–212 (2007).
2. Liu, J.-F., Bregman, J. N., Bai, Y., Justham, S. & Crowther, P. Puzzling accretion onto a black hole in the ultraluminous X-ray source M 101 ULX-1. *Nature* **503,** 500–503 (2013).
3. Feng, H. & Soria, R. Ultraluminous X-ray sources in the Chandra and XMM-Newton era. *New Astron. Rev.* **55,** 166–183 (2011).
4. Feng, H., Rao, F. & Kaaret, P. Discovery of millihertz X-ray oscillations in a transient ultraluminous X-ray source in M82. *Astrophys. J.* **710,** L137–L141 (2010).
5. Skinner, G. K. *et al.* Discovery of 69 ms periodic X-ray pulsations in A0538–66. *Nature* **297,** 568–570 (1982).
6. Lucke, R., Yentis, D., Friedman, H., Fritz, G. & Shulman, S. Discovery of X-ray pulsations in SMC X-1. *Astrophys. J.* **206,** L25–L28 (1976).
7. Kouveliotou, C. *et al.* A new type of transient high-energy source in the direction of the Galactic Centre. *Nature* **379,** 799–801 (1996).
8. Basko, M. M. & Sunyaev, R. A. The limiting luminosity of accreting neutron stars with magnetic fields. *Mon. Not. R. Astron. Soc.* **175,** 395–417 (1976).
9. Gnedin, Y. N. & Sunyaev, R. A. The beaming of radiation from an accreting magnetic neutron star and the X-ray pulsars. *Astron. Astrophys.* **25,** 233–239 (1973).
10. Basko, M. M. & Sunyaev, R. A. Radiative transfer in a strong magnetic field and accreting X-ray pulsars. *Astron. Astrophys.* **42,** 311–321 (1975).
11. Harrison, F. A. *et al.* The Nuclear Spectroscopic Telescope Array (NuSTAR) high-energy X-ray mission. *Astrophys. J.* **770,** 103–122 (2013).
12. Kaaret, P. *et al.* Chandra High-Resolution Camera observations of the luminous X-ray source in the starburst galaxy M82. *Mon. Not. R. Astron. Soc.* **321,** L29–L32 (2001).
13. Kaaret, P., Simet, M. G. & Lang, C. C. A 62 day X-ray periodicity and an X-ray flare from the ultraluminous X-ray source in M82. *Astrophys. J.* **646,** 174–183 (2006).
14. Kong, A. K. H., Yang, Y. J., Hsieh, P. Y., Mak, D. S. Y. & Pun, C. S. J. The ultraluminous X-ray sources near the center of M82. *Astrophys. J.* **671,** 349–357 (2007).
15. Ransom, S. M. *New Search Techniques for Binary Pulsars.* PhD thesis, Harvard Univ. (2001).
16. Bildsten, L. *et al.* Observations of accreting pulsars. *Astrophys. J. Suppl. Ser.* **113,** 367–408 (1997).
17. Canuto, V., Lodenquai, J. & Ruderman, M. Thomson scattering in a strong magnetic field. *Phys. Rev. D* **3,** 2303–2308 (1971).
18. Pringle, J. E. & Rees, M. J. Accretion disc models for compact X-ray sources. *Astron. Astrophys.* **21,** 1–9 (1972).
19. Ghosh, P. & Lamb, F. K. Accretion by rotating magnetic neutron stars. III — Accretion torques and period changes in pulsating X-ray sources. *Astrophys. J.* **234,** 296–316 (1979).

Author Contributions M.B., reduction and timing analysis of the NuSTAR observations, interpretation of results, manuscript preparation; F.A.H., interpretation of results, manuscript preparation; D.J.W., NuSTAR and Chandra spectroscopy, point source analysis; B.W.G., NuSTAR image analysis; D.C., accretion torque analysis, interpretation; F.F., verification of timing analysis, interpretation; D.B., A.B., A.C.F., A.H., V.M.K., T.M., J.T., interpretation of results and manuscript review; S.B., F.C., W.W.C., C.J.H., D.S., S.P.T., N.W., W.W.Z., manuscript review.

Author Information Reprints and permissions information is available at www.nature.com/reprints. The authors declare no competing financial interests. Readers are welcome to comment on the online version of the paper. Correspondence and requests for materials should be addressed to M.B. (mbachett@oa-cagliari.inaf.it) and F.A.H. (fiona@srl.caltech.edu).

METHODS

Observations and preliminary data reduction. NuSTAR[11] observed the M82 field 7 times between 2014 January 23 and 2014 March 06 (see Extended Data Table 1 for details), for a total exposure of 1.91 Ms. We used the NuSTAR data analysis software (NuSTARDAS) version 1.2.0 and NuSTAR CALDB version 20130509 with the standard filters to obtain good time intervals, excluding the periods where the source was occulted by the Earth or was transiting through the South Atlantic Anomaly. NuSTAR records event arrival times with a resolution of 10 μs. Clock drifts, mostly due to temperature, are recorded at each ground station passage into a clock correction file that is updated monthly. The final time accuracy that can be reached by applying these clock corrections is ∼2 ms. We applied these corrections to obtain Solar System barycentre corrected event times using the general-purpose FTOOL barycorr and the NuSTAR clock correction file (v030).

Chandra[20] observed the M82 field using the ACIS-S detector in timed exposure (TE)/VFAINT mode between 2014-02-13 20:09:32 and 2014-02-04 14:50:00 for a total exposure of 47 ks. We reduced the data with the standard pipeline in the Chandra Interactive Analysis of Observations software package (CIAO, version 4.6), filtering the data for periods of high background to produce a cleaned event list. We extracted point source spectra from circular regions of radius ∼1–2″, depending on the proximity of other nearby sources, while the background was estimated from a larger region of radius ∼35″, free of contaminating point sources and away from the plane of the M82 galaxy. Spectra and instrumental responses were produced from the cleaned events with the CIAO SPECEXTRACT tool, and were corrected for the fraction of the PSF falling outside the source region.

The primary goal of the Chandra observation was to constrain any faint soft X-ray emission from the recent SN 2014J[21], and so the observation was performed with the maximum frame-time of 3.2 s. Unfortunately, the two ULXs in M82 (X-1 and X-2) are sufficiently bright that the long frame integration time resulted in the Chandra spectra from these sources suffering from fairly severe pileup[22] (pileup refers to the scenario in which more than one photon is incident on a detector pixel within one frame time, resulting in the spurious apparent detection of a single photon with the combined energy of the individual incident photons). The detected counts-per-frame is ∼0.45 for both X-1 and X-2, which equates to a pileup fraction of ∼20–30% based on the Chandra ABC guide to pileup (http://cxc.harvard.edu/ciao/download/doc/pileup_abc.pdf). This unfortunately prevents a straightforward estimation of the fluxes of these two sources from the Chandra data alone. We will return to this issue below. None of the other point sources are bright enough to suffer significantly from these effects.

There is a known flux calibration discrepancy of ∼10% between NuSTAR and Chandra. We account for this discrepancy, and quote fluxes based on the NuSTAR zeropoint.

Swift monitored the field of SN 2014J regularly from 2014 January 23 through to the end of 2014 April. We reduced the data using the Swift mission automated data analysis server[23].

Timing analysis. To determine the mean period and orbital parameters we divided the observations into overlapping 30-ks intervals and ran an accelerated epoch folding search[15] in each interval. To do this we used the software PRESTO[15], originally designed for radio observations of pulsars. To adapt the NuSTAR data to this software we modified the makebininf script by Abdo and Ray, originally written to use PRESTO with data from the Fermi satellite. To assess the quality of detection, accounting for possible difference in statistics between radio and X-ray data, we ran the same search with a random distribution of initial guesses for the period, far from the observed pulse period, and looked at the distribution of σ for the 'best detections'. More than 99% of false detections were below a PRESTO value of 8σ, which we use to define an acceptable detection. With this criterion we detected pulsations over ∼10 days of observations. We cross-checked the detection with independent software using ISIS[24].

The observed pulse period exhibits sinusoidal variations resulting from the binary orbital motion. Assuming a circular orbit, the observed period p_{obs} varies according to $p_{obs} = p_{em}\{1 + X\Omega \sin[\Omega(t - T_{90})]\}$, where p_{em} is the period in the system of reference co-moving with the pulsar, X is the projected semi-major axis of the orbit in light seconds, $\Omega = 2\pi/P_{orb}$ is the orbital angular velocity and T_{90} is the time of longitude 90° (or mid-eclipse) assuming the ascending node is at longitude 0.

During ObsIDs 008–009, the interval over which we fit for the orbital parameters, we find an additional trend in the phases which requires a period derivative $\dot{P} \approx -2 \times 10^{-10}$ s s⁻¹. NuSTAR's relative timing accuracy is currently known to ∼2 ms over time intervals comparable to these observations. There is evidence for clock drifts of ∼0.4 ms on the ∼97 min orbital timescale. Taking this drift into account, the observed period could have a systematic error of up to ∼10⁻⁷ s. This is orders of magnitude below the observed trend (∼0.1 ms) that we associate with a period derivative.

The ephemeris determined above is not sufficiently precise to align the pulses throughout any of the observations. In order to refine it, we calculated times of arrival

(TOA) of the pulsations in each 30 ks interval and searched for an ephemeris that connects their phases[25]. To do this, we used the software Tempo2[26]. We found an orbital solution that aligns the TOAs to better than 36 ms (r.m.s.) from MJD 56696 to MJD 56701, the interval with the most significant detections.

We looked for signatures of eccentricity using the ELL1 model in Tempo2, adequate for low eccentricity orbits. We used TOAs calculated on different time-scales (from 10 ks to 40 ks) in order to account for possible timescale-related effects. We measured values of the eccentricity that were always consistent with 0 within 2σ, with a maximum eccentricity of 0.002. We used this estimate to obtain a rough upper limit on the eccentricity of 0.003. The parameters of this orbital solution (determined for ObsIDs 008–009) can be found in Extended Data Table 2. Since the orbit is circular, we used the convention $T_0 = T_{asc}$ and so $T_{90} = T_{asc} + P_{orb}/4$, where T_0, T_{asc} and T_{90} are the times of passage through periastron, ascending node and mean longitude 90° respectively.

We found that the above ephemeris was not valid before MJD 56696, with the residuals from the best fit rapidly departing from 0. Therefore, for the rest of the ObsIDs, we used PRESTO with the previously determined orbital solution, and searched the period–$\dot{p}$ plane for more precise solutions inside individual ObsIDs. We determined values of period and period derivative that align the pulsation to better than 10% of the period inside single ObsIDs. By using each of these newly determined ephemerides as a first approximation and propagating to the earlier observation, we were able to detect the pulsation on a much longer interval, including the whole of ObsID 006. These local solutions are summarized in Extended Data Table 3, and are the used for the phase-resolved analysis below.

We looked for any modulation of the phases at the orbital frequency (or harmonics) that might hint at poorly determined orbital parameters or yet-unmodelled orbital parameters (for example, eccentricity, orbital period decay). We first subtracted the long-term trend of the phases with an *ad hoc* function, as implemented in Tempo2. The residuals of this curve have an erratic behaviour with quite large departures from a constant on timescales of several days. We calculated the Lomb-Scargle periodogram[27] of the residuals, looking for significant signatures at the orbital period or factors. We found no significant modulations of this kind. This timing noise is therefore not of orbital origin.

Counterpart identification. Chandra imaging: Extended Data Fig. 1 shows an image of the central region of M82 from Chandra in the 0.3–10 keV band made from the observation coincident with NuSTAR ObsID 006. Given the pileup issues suffered by X-1 and X-2, we focus here on estimating fluxes from the rest of the point source population. Spectra are extracted for each source individually following the method outlined above. Given that these sources are mostly rather faint, we systematically rebin their spectra to have a minimum of 5 counts per bin, and minimize the Cash statistic[28] when analysing these data. All spectral analysis is performed with XSPEC v12.8.1[29], and unless stated otherwise, quoted parameter uncertainties are the 90% confidence intervals for one parameter of interest.

We fit each source with two simple spectral models, the first an absorbed power law and the second an absorbed accretion disk (DISKBB[30] in XSPEC), focusing on the 1–10 keV bandpass to minimize the effects of the strong diffuse plasma emission from the M82 galaxy[31], which peaks at very low energies. When applying the former model, we limit the photon index to be positive, and for the latter model, we limit the disk temperatures to be less than 5 keV. These simple models provide good phenomenological descriptions of the data for the majority of the sources, the only exception being source 15, and we compute fluxes from the 3–10 keV bandpass for each (that is, the common bandpass between Chandra and NuSTAR). For source 15, the Chandra data strongly require a second, soft X-ray component, and we additionally include a low temperature thermal plasma, modelled with the MEKAL code[32], assuming solar abundances), and compute 3–10 keV fluxes based on these models. These Chandra fluxes are compared to the total NuSTAR flux in the 3–10 keV bandpass of $(1.50 \pm 0.03) \times 10^{-11}$ erg cm⁻² s⁻¹, which we compute with a phenomenological combination of a Gaussian iron Kα emission line and a Comptonized continuum model (CompTT[33]) fitted to the portion of the NuSTAR data simultaneous with the Chandra observation, extracted from the 70″ region shown in Extended Data Fig. 1.

Extended Data Table 4 provides the results of the power-law fits for the brightest five sources in this population. The disk-blackbody fluxes are typically within 30% of the powerlaw results (the latter generally being higher). Even taking the conservative approach and adopting the slightly higher powerlaw fluxes, none of these sources contribute more than 5% of the 3–10 keV NuSTAR flux. Given the observed 3–10 keV pulse fraction at the time of the Chandra observation, it is clear that only X-1 and X-2 are bright enough to be the origin of these pulsations.

NuSTAR astrometry: we use the 'persistent' emission to determine an absolute astrometric correction, which we then apply to the 'pulse-on' images to determine the location of the pulsed emission. We assume that the persistent emission is composed equally of emission from M82 X-1 and X-2 since the contemporaneous Chandra imaging shows that these dominate the image and have comparable flux. To eliminate contamination from diffuse soft X-ray emission, we limit the image to the

energy range from 10 to 40 keV. We find that we can align the NuSTAR image with the mean position of M82 X-1 and X-2 by applying a shift in the image plane of two sky pixels (which have a plate scale of 2.45 arcsec per pixel), which is a reasonable shift given NuSTAR's astrometric accuracy[11].

After astrometric alignment we use the gcntrd.pro routine from the IDL AstroLib to determine the position of the pulsed emission using data within 30 arcsec of the peak brightness. This represents a net sample of 2,500 counts in the subtracted image.

To assess the statistical uncertainty on the source centroid, we perform a Monte Carlo simulation that distributes 2,500 counts in a simulated image according to the on-axis NuSTAR PSF. For each Monte Carlo run we compute the centroid as above and compare the result with the (known) input source location. The X and Y offset distributions from the Monte Carlo have means of 0 and 1σ widths of 0.235 pixels (0.577 arcsec), corresponding to a 90% confidence interval of ± 0.95 arcsec in both X and Y.

The resulting right ascension (α)/declination (δ) centroid of the NuSTAR pulsed image is $\alpha = 09$ h 55 min 51.05 s, $\delta = +69° 40' 47.9''$, J2000, with a combined statistical and systematic error of $\pm 5''$ in the projected image plane.

Swift imaging: we perform imaging analysis on Swift observations made during ObsIDs 007 and 009, when pulsations are detected and the flux from the region is high (see Fig. 1). We use the Swift-XRT automated data processing pipeline[23], obtaining all observations from UT 2014 February 02 through 2014 February 11 and producing an image in the 5–10 keV band (Extended Data Fig. 2, left). We then compare this to the Swift snapshot observations extracted from 2014 March 07 through 2014 March 11 that occurred just after the ObsID 011, when the flux from the NuSTAR extraction region containing M82 X-1 and X-2 had decreased by 40%, but pulsations were still detected. When the flux is high the Swift imaging shows significant contributions from both M82 X-2 and X-1, but after ObsID 011 M82 X-2 is dominant in the Swift images. This is consistent with a significant decrease in flux of M82 X-1. The continued detection of pulsations indicates that they originate from M82 X-2.

Flux measurements and spectroscopy of M82 X-1 and M82 X-2. We estimate the 3–10 keV flux from M82 X-2 during our observations from the Chandra observation. As noted previously, the Chandra data for X-2 are quite piled-up, which results in strong degeneracies in the flux inferred from these data alone. By including the NuSTAR data, which does not suffer from these effects, it is possible to break this degeneracy. Since the NuSTAR aperture is much larger than the aperture used for the Chandra data, it includes the emission from a variety of other point sources, including X-1 (for which the Chandra data are also piled-up, resulting in similar issues), and also much of the diffuse M82 plasma emission. The contribution of these additional sources of emission to the NuSTAR data need to be accounted for before the flux of X-2 can reliably be estimated from the combined data set. Throughout all our analysis, we include a neutral absorption component fixed at the Galactic column in the direction of M82[34] ($N_H = 5.04 \times 10^{20}$ cm^{-2}) and additionally allow for variable neutral absorption intrinsic to M82.

Diffuse emission: we assess the contribution from the diffuse plasma emission, and extract an integrated Chandra spectrum from the $70''$ NuSTAR aperture with SPECEXTRACT, excluding all the point sources identified in Extended Data Fig. 1. For the subsequent analysis, we follow ref. 31. We leave a detailed analysis of the diffuse emission during this observation for future studies; for our purposes, it is only important that a phenomenological model with three hot diffuse gas (MEKAL Xspec model) components provides a good description of the data. We find that this diffuse emission contributes (20 ± 1)% of the observed 3–10 keV NuSTAR flux.

Other point sources: we model the emission from the additional X-ray source population (that is, excluding X-1 and X-2) for inclusion in the joint fitting. None of these sources are bright enough to significantly suffer from pileup. We first focus on the brightest two sources from this additional X-ray population, sources 15 and 18, and fit their full 0.3–10.0 keV Chandra spectra with a phenomenological model composed of a low-temperature MEKAL plasma (to account for the diffuse emission) and an accretion disk continuum.

For the rest of the fainter point source population, we combine their lower quality individual Chandra spectra into a single average spectrum, and simply model this to determine their contribution. We apply the same accretion disk continuum model used above. The total contribution from point sources other than X-1 and X-2 is found to be (17 ± 1)% of the observed 3–10 keV NuSTAR flux.

M82 X-1 and X-2: having characterized all the other sources of emission in the NuSTAR aperture, we can now constrain the fluxes of X-1 and X-2 (given the pileup issues in the Chandra data, both sources need to be analysed in this fashion simultaneously). We construct a 'contamination' model for the NuSTAR data obtained simultaneously with the Chandra observation, which is the sum of our characterizations of the diffuse emission and the other point sources, described above. The parameters of this contamination model are all set to the best-fit values obtained in our separate analysis of these various emission components, and are not allowed to vary.

To this model, we add two additional continuum components to represent X-1 and X-2, both absorbed. For the continuum, we use the CompTT model, as with different parameter combinations this model has the flexibility to provide both powerlaw-like and blackbody-like spectra, as required by the data. We then construct the same CompTT models for the Chandra data for X-1 and X-2 individually, and link the parameters for these components between the NuSTAR and the respective Chandra spectra. Finally, the Chandra models are modified by a pileup kernel[22], which accounts for the spectral distortions introduced by these effects. The influence of these effects, characterized by the grade migration parameter α (ref. 22), is not known a priori, and is free to vary independently for X-1 and X-2. Although this pileup kernel can introduce strong degeneracies in the intrinsic flux inferred, this simultaneous modelling of the NuSTAR and the Chandra data, and the careful modelling of all the other sources of emission in the NuSTAR aperture, allows us to account for the pileup in the Chandra data, while also requiring that the total flux does not exceed that in the NuSTAR aperture, breaking this flux degeneracy.

With this approach, we find that the 3–10 keV fluxes of X-1 and X-2 are relatively similar during this Chandra observation, contributing 42^{+3}_{-4}% and 21^{+2}_{-1}% of the 3–10 keV NuSTAR flux, corresponding to 3–10 keV luminosities of $(10 \pm 1) \times 10^{39}$ erg s^{-1} and $4.9^{+0.6}_{-0.3} \times 10^{39}$ erg s^{-1} respectively (for a distance to M82 of 3.6 Mpc). Using the measured spectrum and absorption column, we find an unabsorbed 0.5–10 keV luminosity of 6.6×10^{39} erg s^{-1} for X-2.

20. Weisskopf, M. C. et al. An overview of the performance and scientific results from the Chandra X-ray observatory. Publ. Astron. Soc. Pacif. **114,** 1–24 (2002).
21. Goobar, A. et al. The rise of SN 2014J in the nearby galaxy M82. Astrophys. J. **784,** L12 (2014).
22. Davis, J. E. Event pileup in charge-coupled devices. Astrophys. J. **562,** 575–582 (2001).
23. Evans, P. A. et al. Methods and results of an automatic analysis of a complete sample of Swift-XRT observations of GRBs. Mon. Not. R. Astron. Soc. **397,** 1177–1201 (2009).
24. Houck, J. C. & Denicola, L. A. ISIS: an Interactive Spectral Interpretation System for high resolution X-ray spectroscopy. Astron. Data Analysis Softw. Syst. **216,** 591–594 (2000).
25. Blandford, R. & Teukolsky, S. A. Arrival-time analysis for a pulsar in a binary system. Astrophys. J. **205,** 580–591 (1976).
26. Edwards, R. T., Hobbs, G. B. & Manchester, R. N. TEMPO2, a new pulsar timing package — II. The timing model and precision estimates. Mon. Not. R. Astron. Soc. **372,** 1549–1574 (2006).
27. Scargle, J. D. Studies in astronomical time series analysis. II — Statistical aspects of spectral analysis of unevenly spaced data. Astrophys. J. **263,** 835–853 (1982).
28. Cash, W. Parameter estimation in astronomy through application of the likelihood ratio. Astrophys. J. **228,** 939–947 (1979).
29. Arnaud, K. A. XSPEC: the first ten years. Astron. Data Analysis Softw. Syst. **101,** 17–20 (1996).
30. Mitsuda, K. et al. Energy spectra of low-mass binary X-ray sources observed from TENMA. Astron. Soc. Jpn **36,** 741–759 (1984).
31. Ranalli, P., Comastri, A., Origlia, L. & Maiolino, R. A deep X-ray observation of M82 with XMM-Newton. Mon. Not. R. Astron. Soc. **386,** 1464–1480 (2008).
32. Mewe, R., Gronenschild, E. H. B. M. & van den Oord, G. H. J. Calculated X-radiation from optically thin plasmas. V. Astron. Astrophys. Suppl. Ser. **62,** 197–254 (1985).
33. Titarchuk, L. Generalized Comptonization models and application to the recent high-energy observations. Astrophys. J. **434,** 570–586 (1994).
34. Kalberla, P. M. W. et al. The Leiden/Argentine/Bonn (LAB) survey of Galactic HI. Final data release of the combined LDS and IAR surveys with improved stray-radiation corrections. Astron. Astrophys. **440,** 775–782 (2005).
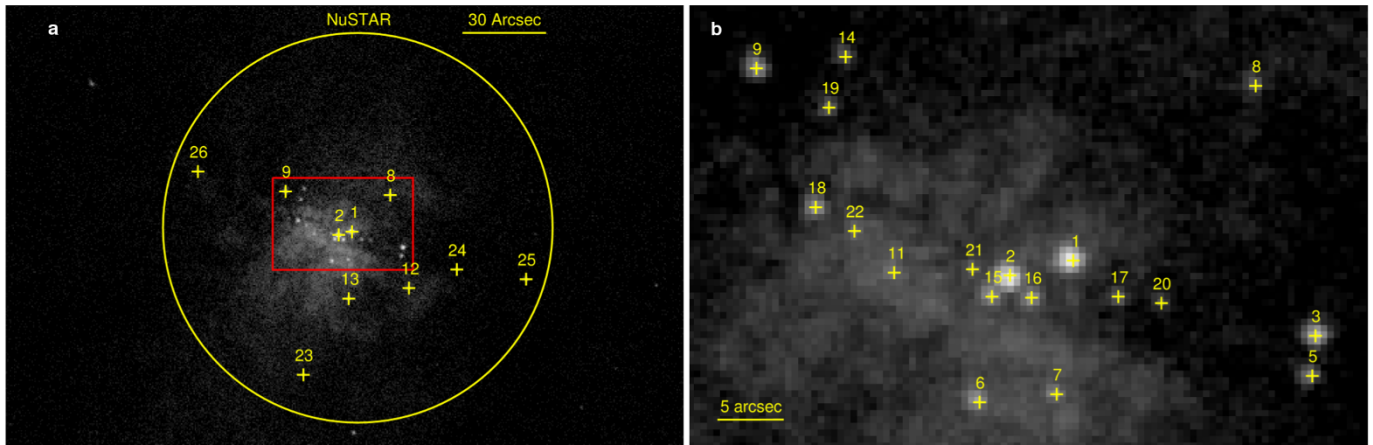
Extended Data Figure 1 | X-ray sources identified by Chandra in the central region of M82. a, Chandra image of the central region of M82 from the observation taken coincident with NuSTAR ObsID 006. The yellow circle shows the 70″ radius region used to extract NuSTAR fluxes. Within this region, 24 discrete X-ray point sources are identified, including X-1 and X-2.

b, Expanded view of the crowded central region of **a**. Yellow crosses indicate the locations of identified point sources. We have used, where possible, the numbering from ref. 13 (sources up to no. 15). After this we assign our own numerical identification (note that sources 4 and 10 from ref. 13 are not detected in this observation).
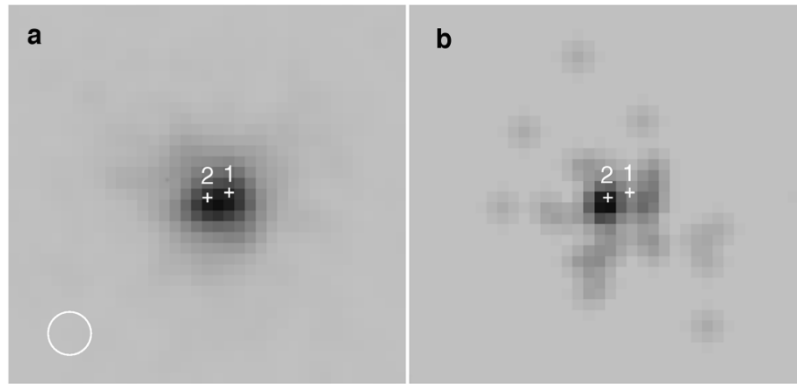
Extended Data Figure 2 | Swift imaging of the region containing M82 X-1 and M82 X-2. a, b, In greyscale are images obtained via Swift automated processing over the 5–10 keV band for all of the observations during early February (**a**; 2014 February 04 through 2014 February 11) and mid-March (**b**; 2014 March 7 through 2014 March 11). The early February observations have 68.5 ks of exposure (mostly because of the increased cadence of observations due to the Swift monitoring of SN 2014J), while the mid-March snapshot has 1.8 ks of exposure. The images are 1.5 arcmin on a side and have been smoothed with a 2-pixel (4 arcsecond) Gaussian kernel (circle at lower left). The location of X-1 and X-2 are shown by the crosses in both panels. The late-time observation clearly shows a reduction in the flux from X-1 and that the flux is dominated by X-2.

Extended Data Table 1 | List of NuSTAR observations used in this analysis

ObsId	Date start (UT)	Date end (UT)	Effective Exposure (ks)
80002092002	2014-01-23 12:58:00	2014-01-24 23:01:05	65.818
80002092004	2014-01-25 19:53:58	2014-01-27 19:16:03	89.965
80002092006	2014-01-28 12:31:46	2014-02-04 05:29:48	309.525
80002092007	2014-02-04 06:07:53	2014-02-10 18:14:28	306.24
80002092008	2014-02-10 18:51:40	2014-02-11 12:00:24	33.648
80002092009	2014-02-11 12:37:59	2014-02-13 23:45:23	114.893
80002092011	2014-03-03 17:07:14	2014-03-06 01:02:13	110.925

Start and stop dates are given, as is the effective exposure of each observation. The exposure has been corrected for the period during which the source was occulted by the Earth, periods during which the instrument was not taking data and for the rate-dependent deadtime when the instrument was processing events and not sensitive to new incident photons.

Extended Data Table 2 | Best-fit orbital parameters

Parameter	Value
Orbital period P_{orb} (d)	2.53260(5)
Projected semi-major axis X (ls)	22.225(4)
Mid-eclipse time T_{90} (MJD)	56695.3659(1)

Orbital parameters determined by fitting a sinusoidal orbital modulation to ObsIDs 008–009. Error ranges for the parameters are given at the 1σ level.

Extended Data Table 3 | Best fit period and period derivatives for individual NuSTAR observations

ObsId	MJD	Period (s)	Period derivative (s/s)	Period 2nd derivative (s/s^2)	TOA Scatter (ms)
006	56685.5	1.3726001(4)	$-3.0(1) \times 10^{-11}$	0	62
007	56692.2	1.3725728(4)	$8(3) \times 10^{-12}$	$-4.2(1) \times 10^{-16}$	31
008-009	56698.7	1.3725076(4)	$-1.38(7) \times 10^{-10}$	$-3.3(5) \times 10^{-16}$	9
011	56719.8	1.3722225(6)	$-2.73(7) \times 10^{-10}$	0	14

Pulse period and period derivatives fitted to time of arrival (TOA) data for individual observations after removal of the orbital modulation. Errors are 1σ, and the parentheses indicate the error on the last digit of the reported value.

Extended Data Table 4 | 3–10 keV flux contributions for bright sources near the nucleus of M82

Source	N_H (10^{22} cm^{-2})	Γ	3-10 keV flux contribution (%)
15	50^{+10}_{-20}	3 ± 1	4.4 ± 0.6
18	3 ± 1	0.4 ± 0.3	4.2 ± 0.6
9	6 ± 1	2.8 ± 0.4	1.3 ± 0.2
6	0.5 ± 0.3	1.6 ± 0.2	1.2 ± 0.2
20	2^{+4}_{-1}	< 1.0	$1.0^{+0.2}_{-0.4}$

Fluxes derived from power-law fits to the five brightest sources after M82 X-1 and X-2. Errors are 90% confidence. N_H is the hydrogen column and Γ is the power-law index.